

# **On the influence of the vascular architecture on Gradient Echo and Spin Echo BOLD fMRI signals across cortical depth: a simulation approach based on realistic 3D vascular networks**

Mario Gilberto Báez-Yáñez<sup>1</sup>, Jeroen C.W. Siero<sup>1,3</sup>, Vanja Curcic<sup>1</sup>, Matthias J.P. van Osch<sup>2</sup> and Natalia Petridou<sup>1</sup>

<sup>1</sup>Translational Neuroimaging Group, Center for Image Sciences, University Medical Center Utrecht, Utrecht, the Netherlands

<sup>2</sup>C.J. Gorter MRI Center, Department of Radiology, Leiden University Medical Center, Leiden, the Netherlands

<sup>3</sup>Spinoza Centre for Neuroimaging Amsterdam, Amsterdam, the Netherlands.

## **Correspondence to:**

Mario G. Báez-Yáñez, PhD

email: [M.G.Baez-Yanez-2@umcutrecht.nl](mailto:M.G.Baez-Yanez-2@umcutrecht.nl) ; [mbaezy88@gmail.com](mailto:mbaezy88@gmail.com)

Translational Neuroimaging Group, Center for Image Sciences, University Medical Center Utrecht, Room Q.02.4.307, Heidelberglaan 100, 3584 CX, Utrecht, Netherlands, tel: +31 (0) 88 75 50919

## **RUNNING HEADLINE**

Vascular architecture influences laminar BOLD

**TOTAL WORDS: ----**

## ABSTRACT

GE-BOLD contrast stands out as the predominant technique in functional MRI experiments for its high sensitivity and straightforward implementation. GE-BOLD exhibits rather similar sensitivity to vessels independent of their size at submillimeter resolution studies like those examining cortical columns and laminae. However, the presence of nonspecific macrovascular contributions poses a challenge to accurately isolate neuronal activity. SE-BOLD increases specificity towards small vessels, thereby enhancing its specificity to neuronal activity, due to the effective suppression of extravascular contributions caused by macrovessels with its refocusing pulse. However, even SE-BOLD measurements may not completely remove these macrovascular contributions. By simulating hemodynamic signals across cortical depth, we gain insights into vascular contributions to the laminar BOLD signal. In this study, we employed four realistic 3D vascular models to simulate oxygen saturation states in various vascular compartments, aiming to characterize both intravascular and extravascular contributions to GE and SE signals, and corresponding BOLD signal changes, across cortical depth at 7T. Simulations suggest that SE-BOLD cannot completely reduce the macrovascular contribution near the pial surface. Simulations also show that both the specificity and signal amplitude of BOLD signals at 7T depend on the spatial arrangement of large vessels throughout cortical depth and on the pial surface.

## 60    **KEYWORDS**

61    7T

62    Computational biophysical modeling

63    Laminar BOLD fMRI

64    Layer fMRI

65    Monte-Carlo simulations

66    Realistic cortical vascular network

67

68

69

70

71

72

73

74

75

76

77

78

79

80

81

82

83

84

85

## 86    **ABBREVIATIONS**

87    3D: three-dimensional

88    7T: 7 tesla

89    BOLD: blood oxygenation level-dependent

90    CBF: cerebral blood flow

91    CBV: cerebral blood volume

92    CMRO<sub>2</sub>: oxygen metabolism

93    CSF: cerebrospinal fluid

94    fMRI: functional magnetic resonance imaging

95    GE: gradient echo

96    GM: grey matter

97    HcT: hematocrit

98    SE: spin echo

99    TE: echo time

100    WM: white matter

101

102

103

104

105

106

107

108

109

110

111

# 1. INTRODUCTION

Functional magnetic resonance imaging (fMRI) has revolutionized our understanding of brain function by allowing noninvasive mapping of brain activity. One of the most used fMRI techniques relies on the blood oxygen level-dependent (BOLD) signal, which is based on the combined effects of changes in local cerebral blood flow (CBF), cerebral blood volume (CBV) and oxygen metabolism (CMRO<sub>2</sub>) upon neuronal activation<sup>1-3</sup>. Due to recent advances in hardware, such as ultra-high magnetic field scanners ( $\geq 7T$ ) and MR data acquisition strategies, the BOLD imaging technique enables the study of brain function at a high level of detail, i.e. at the mesoscopic organization of the cortex. As a consequence, it is now possible to measure BOLD fMRI activation as a function of cortical depth in human cortex and study neuronal activity across different cortical layers<sup>4-17</sup>. These breakthroughs underscore the potential of high-resolution fMRI as a valuable tool for investigating the fundamental processing within cortical micro-circuits and their intricate interactions.

While laminar BOLD fMRI holds great promise for advancing our understanding of cortical function, several challenges remain. Acquiring high-resolution BOLD fMRI data requires careful optimization of imaging parameters to balance spatial resolution, sampling rate, signal-to-noise ratio, and coverage. Laminar fMRI analysis techniques are still being refined, and validation against invasive techniques is necessary to confirm accuracy<sup>18</sup>. Moreover, the BOLD fMRI signal is an indirect measurement of neuronal functioning. The BOLD fMRI signal is a mixture of effects related to hemodynamic changes induced by neurovascular coupling, the vascular architecture within the sampled volume, and the biophysical interaction of oxygenated blood and tissue. Because BOLD fMRI measures neuronal activity through hemodynamics, its ultimate resolution relies on the spatial extent of neuronal-evoked hemodynamic changes, along with how these changes evolve over time<sup>19-21</sup>.

Numerous laminar fMRI studies, with spatial resolutions reaching  $\leq 1\text{mm}$  in all directions, have examined the spatial characteristics of the recorded hemodynamic signals across cortical depth, to enhance our understanding and refine spatial specificity of laminar fMRI<sup>7,13,22-27,57</sup>. Gradient Echo (GE)-BOLD is the most commonly used technique to measure brain activation across cortical depth. Nevertheless, GE-BOLD is sensitive to both macro- and microvascular signal contributions, which impact the specificity of the underlying neuronal activity, especially towards the pial surface. Computational simulations based on mono-sized randomly oriented cylinder models have shown that Spin Echo (SE)-BOLD can minimize the extravascular contribution from large vessels<sup>28-31</sup>. Therefore, SE-BOLD increases the specificity towards the microvasculature and is thus considered to be more specific to the location of neuronal activity<sup>32,33</sup>. However, SE-BOLD fMRI measurements may not completely remove the macrovascular contribution – macrovessels may still influence the detected BOLD signal, especially near the pial surface<sup>23,34</sup> due to several possible factors, such as the impact of the echo planar imaging (EPI) readout<sup>35,36</sup>, the dependence on the echo-time (TE) selection<sup>37</sup> or the different diffusion regimes between the cortical gray matter (GM) and the cerebrospinal fluid (CSF)<sup>30,38</sup>. For that reason, it is necessary to investigate the GE-BOLD and SE-BOLD

signal formation across cortical depth using computational simulations based on realistic 3D cortical vascular networks.

In this work, we used realistic 3D vascular models of mice obtained by two-photon microscopy techniques, with a modified artery-vein ratio in order to mimic human cortical vasculature features, to simulate specific oxygen saturation states and biophysical interactions to characterize the intravascular and extravascular signal contribution of the vascular architectures to the GE-BOLD and SE-BOLD signals across cortical depth. This computational approach can help to understand the influence of the vascular architecture on the GE-BOLD and SE-BOLD signal formation across cortical depth, and the impact of the pulse sequence parameters on the BOLD signal changes at submillimeter acquisitions.

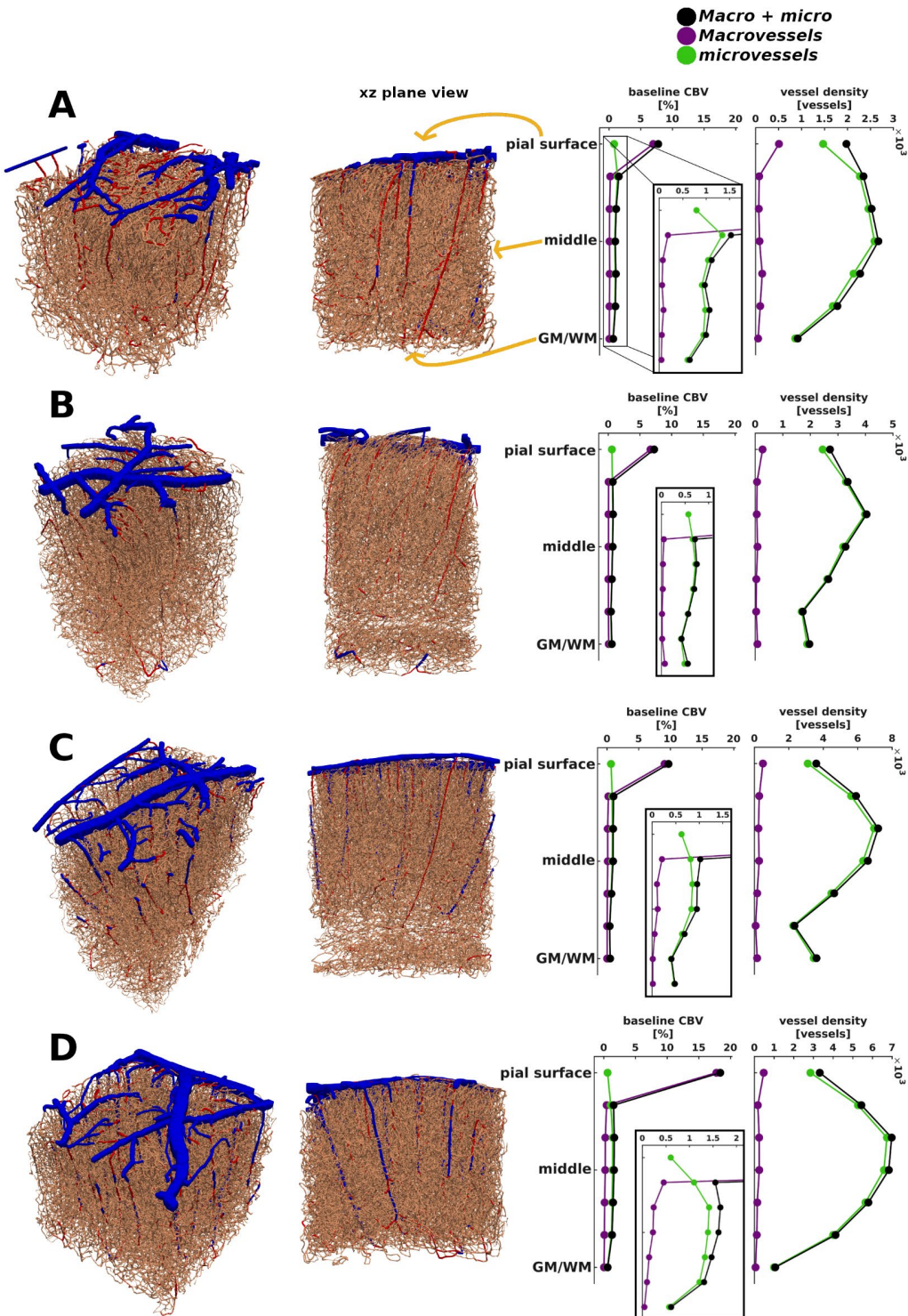
## 2. MATERIAL AND METHODS

### 2.1 Generation of realistic 3D vascular models based on two-photon microscopy data

We utilized four realistic 3D vascular models acquired with two-photon microscopy techniques from the parietal cortex of mice as obtained by Blinder et. al. [2013]<sup>39</sup> (**Figure 1**). Using an in-house MATLAB script, we reconstructed the vasculature using the spatial coordinates of the vessel segments and their associated diameter information. The vascular data, as provided by Blinder et. al. [2013]<sup>39</sup>, was stored in a vectorial structure – where spatial positions comprised an  $m$ -by-3 vector, with  $m$  representing the number of vessels of the vascular model, and two  $m$ -by-1 column vector representing the diameter and length of each vessel segment, respectively. Capillaries are effectively represented by their length and diameter due to their uniform structure. However, arteries and veins, with their intricate shapes, require subdivision into multiple segments to accurately capture their branching patterns, varying diameters, and curvature. More details on the vascular data can be found in Blinder et. al. [2013]<sup>39</sup>.

In this work, vessels smaller than 6 micrometers in diameter were labeled as capillaries<sup>33,40</sup>. To mimic human brain characteristics, the remaining vessels were divided into a 3:1 artery-vein ratio based on diameter. This reflects the 3:1 ratio in humans<sup>41</sup> compared to approximately 1:3 in mice<sup>39,42,43</sup>. Vessels with diameters ranging from 11  $\mu\text{m}$  to 36  $\mu\text{m}$  were designated as veins, constituting the smaller portion, while those with diameters from 6  $\mu\text{m}$  to 11  $\mu\text{m}$  were labeled as arteries<sup>59,60</sup>. Thus, the resulting 3D vascular models included arteries and veins (referred to as macrovessels from here onwards) along with capillaries, small arterioles, and venules (microvessels). The simulated voxel size generated by the vascular models is about 1  $\text{mm}^3$  isotropic. We defined seven cortical layers evenly distributed between the cortical pial surface and the white matter/gray matter (WM/GM) boundaries (see **Figure 1**). It's important to note that these layers were not intended to represent histological laminae or to delineate any vascular features. The number of vessels was computed as the sum of the vessels lying within each of the defined cortical layers. Moreover, the baseline CBV of each cortical layer was computed as the sum of the volume of all its vessels. The volume of a single vessel was calculated from the vessel diameter and length assuming a cylindrical shape.

183



184

185 **Figure 1.** Four realistic 3D vascular models (A-D models) obtained by means of two-photon microscopy  
186 techniques<sup>39</sup>. The realistic vascular models are comprised of three vessel types – arteries in red and veins  
187 in blue (both considered thorough the manuscript as macrovessels), and capillaries, small arterioles, and



venules in beige (considered as microvessels). On the right hand side of each vascular model, baseline CBV and vessel density features are displayed for both macrovessels (purple dotted lines) and microvessels (green dotted lines) – and the total sum in black dotted lines. The models were subsequently used to compute the spatial distribution of frequency shifts assuming different oxygen saturation levels per vascular compartment, and from the frequency shifts the corresponding  $R2^{(*)}$  decay rate effects and the BOLD signal changes are obtained (sections 2.2-4).

## 2.2 Implementation of oxygen saturation levels for each vascular compartment

We simulated different oxygen saturation levels per vascular compartment<sup>53</sup>, which were maintained constant over time, i.e., steady-state oxygen saturation levels were assumed. The baseline oxygen saturation ( $SO_2$ ) values used in each vascular compartment were dependent on the oxygen saturation imposed on the veins, as follows:

- $SO_2$  in arteries ( $SO_{2art}$ ) = 95%;
- $SO_2$  in capillaries =  $SO_{2art} - ((SO_{2art} - SO_{2vein}) / 2)$ ;
- $SO_2$  in veins ( $SO_{2vein}$ ) = [50%, 54%, 59%, 64%, 68%, 73%, 78%, 82%, 87%, 92%].

We extended the simulation oxygen saturation range beyond physiological plausible values (interval that ranges from oxygen saturation values of 60% in the resting state to 80% in the active state), in order to gain a broader understanding of the BOLD signal formation process.

## 2.3 Simulation of the MR signal accounting for intravascular and extravascular signal contributions

BOLD fMRI signals include extravascular and intravascular components, influenced, mainly, by factors like cerebral blood volume and oxygen saturation. The total MR signal was calculated by summing the extravascular signal with both arterial and venous intravascular contributions:

$$MR_{signal} = Extravascular_{signal} + Intravascular_{signal(arteries)} + Intravascular_{signal(veins)} \quad (1)$$

Simulations shown here were computed for gradient echo and spin echo at 7T with an angular orientation of the normal vector arising from the cortical pial surface of the realistic vascular model parallel to the main magnetic field.

### 2.3.1 Simulation of the arterial and venous intravascular signal contribution

In this study, we assumed the intravascular contribution ( $R2^{(*)}_{dHb} = R2^{(*)}_{0,in} + R2_{SO_2}$ ) to the BOLD signal to be non-zero for the arterial and venous compartment. This decision was based on the observation that, at high magnetic fields, the contribution of the arterial and venous compartment tends to be significant at



specific oxygen saturation levels<sup>32,33</sup>. On the other hand, we assumed an intravascular component in the microvascular compartment to be null, given that the  $R2^{(*)}_{dHb}$  of the capillaries has not been well-characterized due to the high heterogeneity in hematocrit levels across the cortical depth<sup>55</sup> and oxygen saturation levels across the capillary bed.

Therefore, we implemented the intravascular arterial and venous contribution for SE as  $1/R2_{0,in} = T2_{0,in}$  ( $\approx 53$  ms)<sup>34</sup>, and  $R2_{SO_2}$  component dependent on oxygen saturation level using the quadratic relation as defined by Uludag et al., [2009]<sup>33</sup>, weighted by the corresponding blood volume fraction (see **Figure 1**). Moreover, we implemented the intravascular arterial and venous contribution for GE as  $1/R2^{*}_{0,in} = T2^{*}_{0,in}$  ( $\approx 10$  ms)<sup>34</sup>, and  $R2_{SO_2}$  component dependent on oxygen saturation level using the relations defined by Uludag et al., [2009]<sup>33</sup>, weighted by the corresponding blood volume fraction (see **Figure 1**).

$$Intravascular_{signal(arteries\ or\ veins)}(t) = (CBV_{arteries\ or\ veins}) \cdot (e^{-R2^{(*)}_{dHb} \cdot t}) \quad (2)$$

Although the intravascular decay rate for both GE and SE is influenced by hematocrit level, we assumed a constant value of hematocrit across vascular compartments in our simulations. This decision aimed to reduce one degree of freedom in the simulations.

### 2.3.2 Simulation of the extravascular signal contribution

The extravascular  $MR_{signal}$  was computed by modelling the interaction of moving spins within the local magnetic field distortions induced by the different oxygen saturation levels<sup>29</sup> (section 2.2). We computed local frequency shifts created by the  $SO_2$  levels of both the macro- and microvascular compartments (**Figure 2**).

The local frequency shift caused by a vessel segment was modeled as the dipolar response of a finite cylinder, presuming negligible effects on the cylinder extremities<sup>44,45</sup>. The local frequency shift  $\delta\omega(r)$  in [1/s] for each vessel segment was computed using:

$$\delta\omega(r) = \frac{1}{2} \cdot \frac{\gamma}{2\pi} \cdot B_0 \cdot \Delta\chi \cdot \left(\frac{R^2}{r^2}\right) \cdot \cos(2\theta) \cdot \sin^2\psi \quad (3)$$

where  $\gamma$  is the hydrogen gyromagnetic ratio = 267.5E6 [rad/(s·T)],  $B_0$  is the main magnetic field (7 [T]),  $\Delta\chi = 4\pi \cdot 0.276$  ppm ·  $HcT \cdot (1 - SO_2)$  [-] is the susceptibility difference produced by the  $SO_2$  in the vessel/cylinder<sup>46</sup> and the hematocrit level  $HcT$  (= 0.45 [-]),  $R$  is the vessel radius in [ $\mu$ m],  $r$  is the Euclidean distance from the center line of the cylinder to a particular spatial position in the simulation volume in [ $\mu$ m],  $\theta$  is the angle between the cylinder and the spatial position in [rad], and  $\psi$  is the angle between the orientation of the cylinder and the main magnetic field in [rad].

The dephasing experienced by a bulk of diffusing spins  $N_{spins}$  was simulated using a Monte Carlo approach (20 repetitions with  $5 \cdot 10^7$  spins each repetition). An ensemble of spins senses the extravascular local

frequency shifts with a diffusion coefficient of  $D = 1 \text{ } [\mu\text{m}^2/\text{ms}]$ , while assuming isotropic diffusion<sup>29</sup>. The calculation of the spin dephasing was obtained through,

$$\varphi(t) = \int_0^t \delta\omega(x(t)) dt \quad (4)$$

where  $\varphi(t)$  is the phase acquired during the simulation time  $t$  and  $\delta\omega(x(t))$  is the local frequency shift at spin position  $x$  at each time-step  $t$ . The phasing experienced for each spin was stored across all simulation time-steps (time step = 0.025 ms). For SE sequences, the acquired phase during the echo time was multiplied by -1 (change in polarity) after TE/2, simulating the effect of the 180-degree refocusing radiofrequency pulse. Using equation (5) we can obtain the normalized extravascular MR signal.

$$Extravascular_{signal}(t) = (1 - CBV_{arteries+veins}) \cdot \left[ \left( \frac{1}{N_{spins}} \sum^{N_{spins}} e^{-i\varphi(t)} \right) \cdot e^{-R2_0^{(*)} \cdot t} \right] \quad (5)$$

Where  $R2_0^{(*)} = 1/T2_0^{(*)}$  is the intrinsic decay rate in cortical tissue, and  $R2'$ , expanded in the term inside the parenthesis, is the decay rate induced by the interaction of the diffusing spins in a local inhomogeneous frequency field. We used the intrinsic tissue  $T2_0^*$  ( $\approx 28 \text{ ms}$ ) relaxation time for GE and the intrinsic tissue  $T2_0$  ( $\approx 50 \text{ ms}$ ) relaxation time for SE according to the nonlinear relationship given by Khajehim et. al. [2017]<sup>47</sup> for cortical gray matter at 7T (see **Table 1**).

To confine spins within the simulation space, voxel boundary conditions were set to infinite space. Spins exiting the voxel re-entered the imaging volume on the opposite side, preserving their magnetization history. However, spins reaching the pial surface and WM/GM boundary were considered invalid iterations and reiterations were performed. Additionally, spin exchange between vascular compartments was prohibited, establishing an impermeable vascular network

## 2.4 GE $R2^*$ and GE BOLD signal change, and SE $R2$ and SE BOLD signal change across cortical depth

The  $MR_{signal}$  and the corresponding GE  $R2^*$  and SE  $R2$  were computed using their respective echo time as described in section 2.3. Given that the behavior of the  $MR_{signal}$  (**Eq. 1**) presents oscillations due to its multi-exponential nature, we simply approximate the  $R2^{(*)}$  decay rate value fitting a polynomial of degree one, i.e. a linear fit, on the natural logarithm of the  $MR_{signal}$ ,  $R2^{(*)} = \frac{\ln(MR_{signal})}{t}$ , for GE and SE, respectively. The BOLD signal change in [%] was defined as the relative change using the 59% oxygen saturation state as the reference / baseline condition ( $SO_{2vein} = 59\%$ ), i.e.,

$$\Delta BOLD = \left( \frac{MR_{signal}(SO_{2vein}, t)}{MR_{signal}(SO_{2vein=59\%}, t)} - 1 \right) \times 100 \quad (6)$$

Hence, we conducted three different experiments/simulations:

1) To quantify the global dephasing effects of GE R2\* and SE R2, we conducted Monte Carlo simulations at the voxel level across the various oxygen saturation states (section 2.2). Additionally, we calculated the GE R2\*/SE R2 ratio as a proxy for vessel size signal contribution<sup>29,48</sup>. Furthermore, we calculated the impact of the extravascular and intravascular signal contribution for different oxygen saturation values for all vascular models.

2) Subsequently, we used Monte Carlo simulations to calculate the contributions of GE R2\* and SE R2, and the corresponding BOLD signal changes, for seven cortical layers. As mentioned above, these cortical layers were evenly defined between the pial surface and the white matter/gray matter (WM/GM) boundaries (see **Figure 1**). Additionally, we calculated the GE R2\*/SE R2 ratio and the ((GE BOLD / SE BOLD) - 1) signal ratio as a proxy for vessel size signal contribution<sup>29,48</sup>.

3) Finally, we simulated the GE R2\* and SE R2 dephasing rate across the seven cortical layers for different echo times ranging from TE = 5 ms to 80 ms with increments of 5 ms. Additionally, we examined the respective BOLD signal changes.

The computational pipeline was implemented using MATLAB and JULIA. The biophysical parameters used to compute the GE R2\* and SE R2, and the respective BOLD signal changes are summarized in **Table 1**.

**Table 1. Biophysical and pulse sequence parameters used to compute a BOLD signal response**

biophysical and MR pulse sequence parameters	
diffusion coefficient (extravascular tissue)	1 $\mu\text{m}^2/\text{ms}$ ; isotropic motion
static magnetic field strength	7 tesla
hematocrit (HcT)	0.45
echo-time (TE) (used in <b>Figure 3 and 4</b> )	gradient echo = 27 ms spin echo = 50 ms
TE range to estimate R2(*) and BOLD signal changes TE-dependency (used in <b>Figure 5 and 6</b> )	5 ms to 80 ms, step of 5ms
time-step	0.025 ms
number of spins	20 Monte-Carlo repetitions with 5·10 <sup>7</sup> spins each repetition
GE: T2 <sub>0</sub> * cortical grey matter at 7T	28 ms
SE: T2 <sub>0</sub> cortical grey matter at 7T	50 ms

GE: intravascular arterial $T_{2\text{dHb}}^*$ at 7T	9 ms @ $\text{SO}_2 = 95\%$
SE: intravascular arterial $T_{2\text{dHb}}$ at 7T	49 ms @ $\text{SO}_2 = 95\%$
GE: intravascular venous $T_{2\text{dHb}}^*$ at 7T	[4, 5, 5.4, 6, 6.7, 7.4, 8, 8.7, 9.3, 9.7] ms @ $\text{SO}_2 = [50\%, 54\%, 59\%, 64\%, 68\%, 73\%, 78\%, 82\%, 87\%, 92\%]$
SE: intravascular venous $T_{2\text{dHb}}$ at 7T	[5, 7, 8.2, 10.1, 12.6, 15.9, 20.6, 26.9, 35, 44.3] ms @ $\text{SO}_2 = [50\%, 54\%, 59\%, 64\%, 68\%, 73\%, 78\%, 82\%, 87\%, 92\%]$

299

300

## 301 **2.5 Validation of computational pipeline through generation of the Boxerman<sup>29</sup> plot**

302 To validate the computational framework, we reproduced results from Boxerman et al. [1995]<sup>29</sup> and Kiselev  
303 et al. [1999]<sup>30</sup>. Using mono-sized randomly oriented cylinders, we computed  $\Delta R_2'$  effects for GE and SE at  
304 1.5T with parameters from Kiselev et al. [1999]<sup>30</sup>. This is shown in **Supplementary Figure 1**. Additionally,  
305 we calculated GE BOLD and SE BOLD signal changes to understand BOLD contrast at 7 Tesla using this  
306 simplified model, detailed in **Supplementary Figure 2**.

307

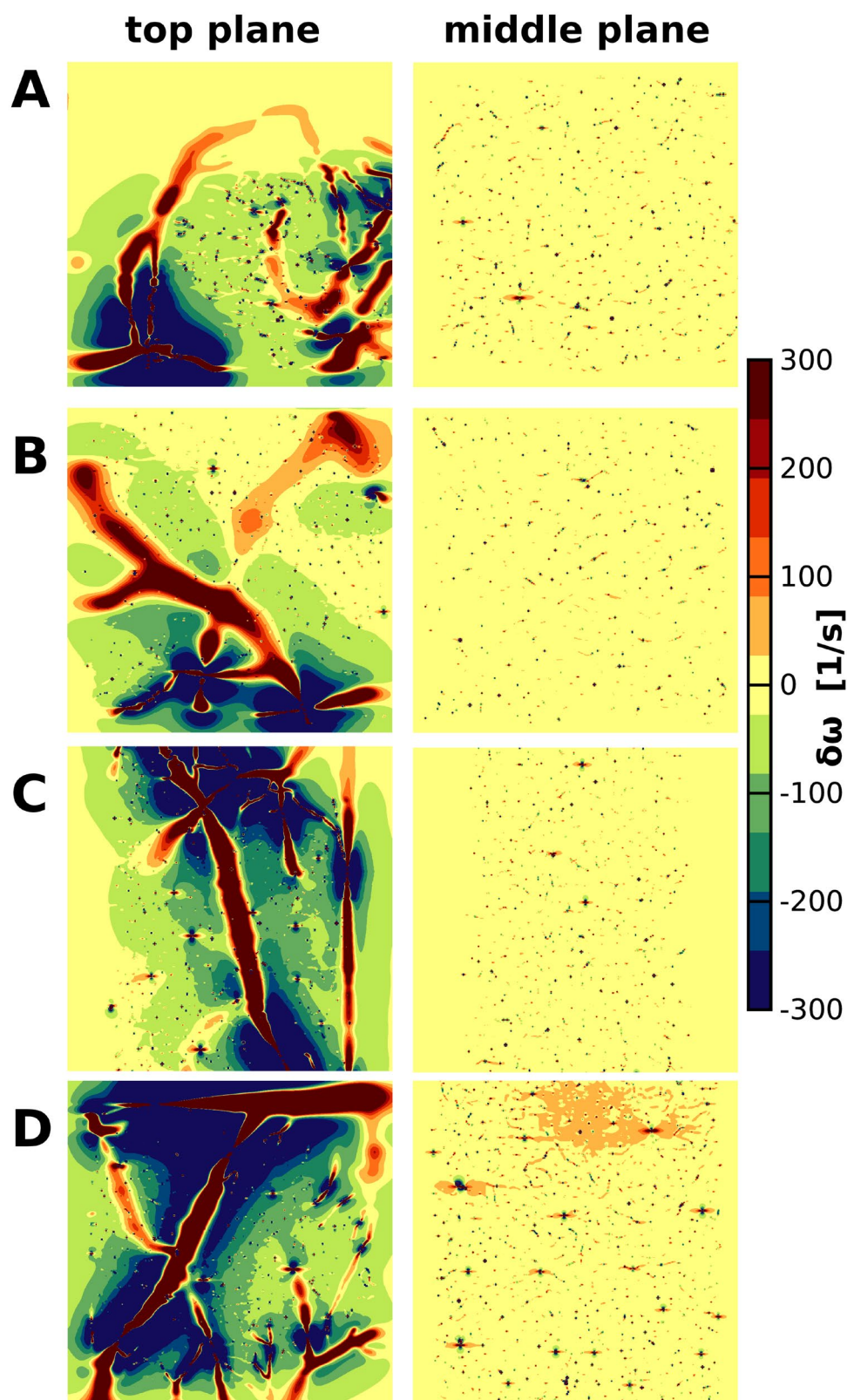
## 308 **3. RESULTS**

309 **Figure 1** illustrates the four vascular models utilized in this study, encompassing arteries, microvessels  
310 (including capillaries, small arterioles/venules), and veins. While obtained from different mice within the  
311 same cortical region (parietal), the capillary beds in all four models demonstrate similar characteristics in  
312 vessel radius, baseline CBV, and vessel density across cortical depth, with somewhat comparable  
313 topologies. However, macrovascular architecture varies among the models, leading to distinct differences  
314 in large vessel organization.

315 The local inhomogeneous frequency shifts produced by the four realistic vascular models for an exemplary  
316 oxygen saturation level ( $\text{SO}_{2\text{vein}} = 78\%$ ) are depicted in **Figure 2**. Two orthogonal planes are depicted:  
317 one approximately 20  $\mu\text{m}$  deep from the cortical surface (top plane), and the other around 500  $\mu\text{m}$  deep  
318 relative to the cortical pial surface (middle plane). Near the cortical surface, significant frequency field  
319 inhomogeneities arise from the macrovasculature, primarily pial veins, with minor contributions from smaller

320 vessels. Conversely, microvessels dominate the middle planes, resulting in slight alterations to the  
 321 frequency field homogeneity, affecting the behavior of moving spins. The distinct macrovascular architecture  
 322 at the pial level creates specific local frequency field signatures, while the middle planes exhibit comparable  
 323 degrees of induced inhomogeneity across the models.

324



325

326 **Figure 2.** Local frequency field distortions produced by the realistic vascular models for an exemplary  
 327 oxygen saturation level ( $SO_{2\text{vein}} = 78\%$ ). The frequency field maps are shown for two different locations



*inside the simulated voxel: the top plane, situated approximately 20  $\mu\text{m}$  in depth from the cortical pial surface, and the middle plane, positioned around 500  $\mu\text{m}$  deep relative to the cortical pial surface. The main magnetic field was simulated to be orthogonal to the cortical pial surface and thus the depicted planes. The unique macrovascular structure of the four vascular models at the pial surface level (top plane) produces a distinctive local spatially inhomogeneous frequency field signature. However, at the middle plane, the vascular architecture is primarily composed of small vessels, leading to a relatively similar degree of induced inhomogeneous frequency field across the models.*

**Figure 3** illustrates the global, i.e. averaged signals over the complete voxel, dephasing in terms of voxel's  $R2^{(*)}$  decay rates using GE (TE = 27 ms) and SE readouts (TE = 50 ms) for the four vascular models. Each solid line in the graphs represents the mean value, while the shaded area represents the 95% confidence interval computed from the repeated Monte Carlo simulations. The grey shaded area covering the oxygen saturation range between 60% to 80% represents the plausible physiological values expected in experimental fMRI data. The horizontal dashed line in **Figure 3a** and **3b** represents the expected  $R2^{(*)}$  in the case where there are no susceptibility differences, i.e., the intrinsic  $R2_0^{(*)}$  of tissue.

All vascular models consistently exhibited a nonlinear response across various oxygen saturation levels (see **Figure 3a** and **3b**). Increasing oxygen saturation within the voxel led to a nonlinear decrease in both GE  $R2^*$  and SE  $R2$  decay rates, with SE  $R2$  showing a more pronounced impact compared to GE  $R2^*$ . Additionally, the confidence interval for SE  $R2$  was slightly larger for low oxygen saturation values compared to higher levels. This difference was not observed in GE  $R2^*$ , where confidence intervals remained similar across all oxygen saturation levels. The ratio between GE  $R2^*$  and SE  $R2$  demonstrated a distinctive wave-like shape (see **Figure 3c**). The lowest point of the curve fell within the plausible physiological range, with values ranging from 1.79 to approximately 2.00, depending on the vascular model. At low oxygen saturation levels ( $\text{SO}_{2\text{vein}} = 50\%$ ), the ratio ranged from 1.89 to 2.15, while at higher levels ( $\text{SO}_{2\text{vein}} = 92\%$ ), it ranged from 1.79 to 2.05. Models A, B, and C exhibited similar GE  $R2^*$  and SE  $R2$  decay rate behaviors, resulting in overlapping and intersecting curves. In contrast, model D showed considerably higher ratio values compared to the other models.

The extravascular, arterial, and venous intravascular contributions to GE and SE signals are depicted in **Figures 3d** and **3e**, with solid lines representing mean values and shaded areas indicating the 95% confidence interval from repeated Monte Carlo simulations across all vascular models. The grey shaded area encompasses oxygen saturation values between 60% to 80%, considered physiologically plausible. The black line represents the extravascular signal component, while the red and blue lines represent arterial and venous intravascular signal components, respectively.

In GE signal contribution, the dominant signal comes from the extravascular compartment (~98% signal contribution), with minimal intravascular contributions from both arterial and venous sources, each less than 2%. Conversely, in the SE signal, intravascular signal contributions, particularly from arterial sources, are



more substantial. Depending on the oxygen saturation level, the arterial component can contribute up to 8%, while the venous component can reach approximately 4%. Consequently, the extravascular compartment constitutes an average signal contribution of about 90% to 95%, depending on the oxygen saturation level.

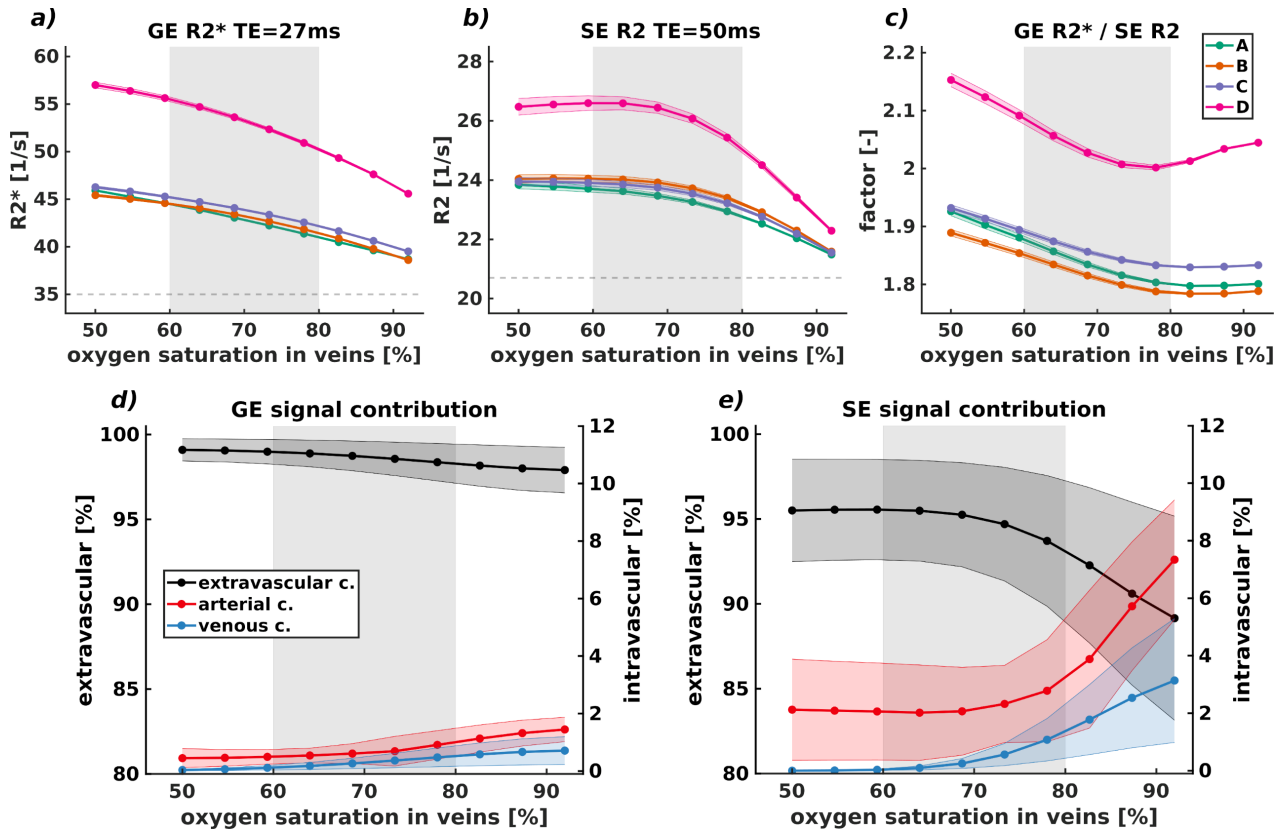


**Figure 3.** Global dephasing, characterized by voxel  $R2^{(*)}$  decay rates, and the extravascular and intravascular contributions to this simulated for GE ( $TE = 27$  ms) and SE ( $TE = 50$  ms) readouts across four vascular models and varying static oxygen saturation values at 7T. Each solid line in the results represents the mean value, while the shaded area in (a), (b) and (c) indicates the 95% confidence interval computed through repeated Monte Carlo simulations, and in (d) and (e) the 95% confidence interval averaged across all vascular models. The grey shaded region, encompassing an oxygen saturation range between 60% to 80%, reflects the plausible physiological values anticipated in human fMRI data. The horizontal dashed line, in (a) and (b), denotes the  $R2^{(*)}$  devoid of susceptibility differences corresponding to the intrinsic  $R2^{(*)}$  of tissue. GE  $R2^*$  (a) shows a larger effect as compared to SE  $R2$  (b). The ratio of GE  $R2^*$  and SE  $R2$  (c) varies between 1.80 to 2.10 in the plausible physiological range. At low oxygen saturation levels ( $SO_{2\text{vein}} = 50\%$ ), the range is approximately from 1.89 to 2.15, while at higher oxygen saturation levels ( $SO_{2\text{vein}} = 92\%$ ), this ratio is approximately in the range from 1.79 to 2.05. The GE  $R2^*$  and SE  $R2$  decay rate behavior for the A, B, and C models displayed largely similar values, resulting in overlapping curves. Conversely, the

*D model featured much higher ratio values as compared to the other models. The contributions of extravascular, arterial, and venous intravascular components to GE and SE signals are depicted in **d)** and **e)**. The black line represents the behavior of the extravascular signal component. The arterial and venous intravascular signal contributions are illustrated by red and blue lines, respectively. In GE signal contribution, the dominant signal originates from the extravascular compartment (~98% signal contribution), whereas both arterial and venous intravascular contributions are minimal. Conversely, in SE signal contribution, the intravascular signal, from both arterial and venous sources, exhibits a more significant contribution compared to GE. Depending on the oxygen saturation level, the arterial component can contribute up to 8% of the signal, while the venous component can contribute up to ~4% and thus the extravascular compartment is reduced -constituting a signal contribution of about ~90%-95% dependent on the oxygen saturation level.*

In **Figure 4**, we illustrate the relationship between the  $R2^{(*)}$  decay rate (panels **a)** to **c)**) and BOLD signal changes (panels **d)** to **f)**) for both GE (TE = 27 ms) and SE (TE = 50 ms) readouts across seven equidistant layers of the cortex for all vascular models. The panels **c)** and **f)** present the resulting GE  $R2^{(*)}$ /SE  $R2$  ratio and the ((GE BOLD / SE BOLD) - 1) signal ratio, respectively. Each solid line in the results represents the mean value, while the shaded area represents the 95% confidence interval computed by the Monte Carlo simulation averaged across all the oxygen saturation levels – where the dashed line represents the boundary produced by the lowest oxygen saturation value and the dotted line represent the boundary given by the highest oxygen saturation value. The independent contribution for each oxygen saturation can be found in **Supplementary Figures 3a** and **Supplementary Figure 3b**. The horizontal dashed line in **a)** and **b)** represents the intrinsic  $R2_0^{(*)}$  of tissue, respectively.

GE  $R2^{(*)}$  decay rates are larger near the cortical pial surface and demonstrates a decreasing trend toward the deeper layers, where most of the  $R2^{(*)}$  contribution comes from the tissue's  $R2_0^{(*)}$  ( $\approx 35.71$  [1/s] accounting for weighted average from extravascular and intravascular CBV and small contributions from  $R2'$ ). SE  $R2$  decay rates exhibit a similar trend as GE  $R2^{(*)}$  (increasing values toward the cortical pial surface) but are smaller due to the refocusing 180-degree pulse - most of the  $R2$  contribution in deeper layers comes from the tissue's  $R2_0$  ( $\approx 20$  [1/s] accounting for weighted average from extravascular and intravascular CBV). However, the refocusing pulse do not entirely eliminate the contribution of large vessels at the pial surface. The factor between GE  $R2^{(*)}$  and SE  $R2$  in deeper layers (panel **c)** towards the WM/GM boundary) is approximately 1.70. Conversely, at the top layers (towards the cortical pial surface), the ratio ranges between approximately 1.90 and 2.25. While GE  $R2^{(*)}$ , SE  $R2$ , and the GE  $R2^{(*)}$ /SE  $R2$  ratio are comparable across the A, B, and C models, the D vascular model exhibited different behavior, showing a pronounced difference in the GE  $R2^{(*)}$ /SE  $R2$  ratio compared to the other models.

Similarly, the BOLD signal change displayed in panels **d)** and **e)** shows higher values near the cortical pial surface (mean GE BOLD: ~30% signal change; SE BOLD: ~15% signal change) compared towards the deeper layers (mean GE BOLD: ~3% signal change; SE BOLD: ~2% signal change). The ratio between GE

BOLD and SE BOLD (panel **f**) demonstrates a similar trend for the A and D model, and comparable ones to the B and C model - ranging between -0.5 and 2.0 depending on the cortical depth and vascular model.

At the cortical pial surface, the ((GE BOLD/SE BOLD) - 1) ratio for all vascular models (panel **f**) are above the reference line. At middle layers, the factor increases to approximately two-fold dependent on the vascular structure - suggesting a large contribution from microvascular and macrovascular compartments. Moreover, at deeper layers, the signal is mostly dominated by the SE readout for all vascular models except the D vascular model - suggesting contribution only from microvascular compartments.

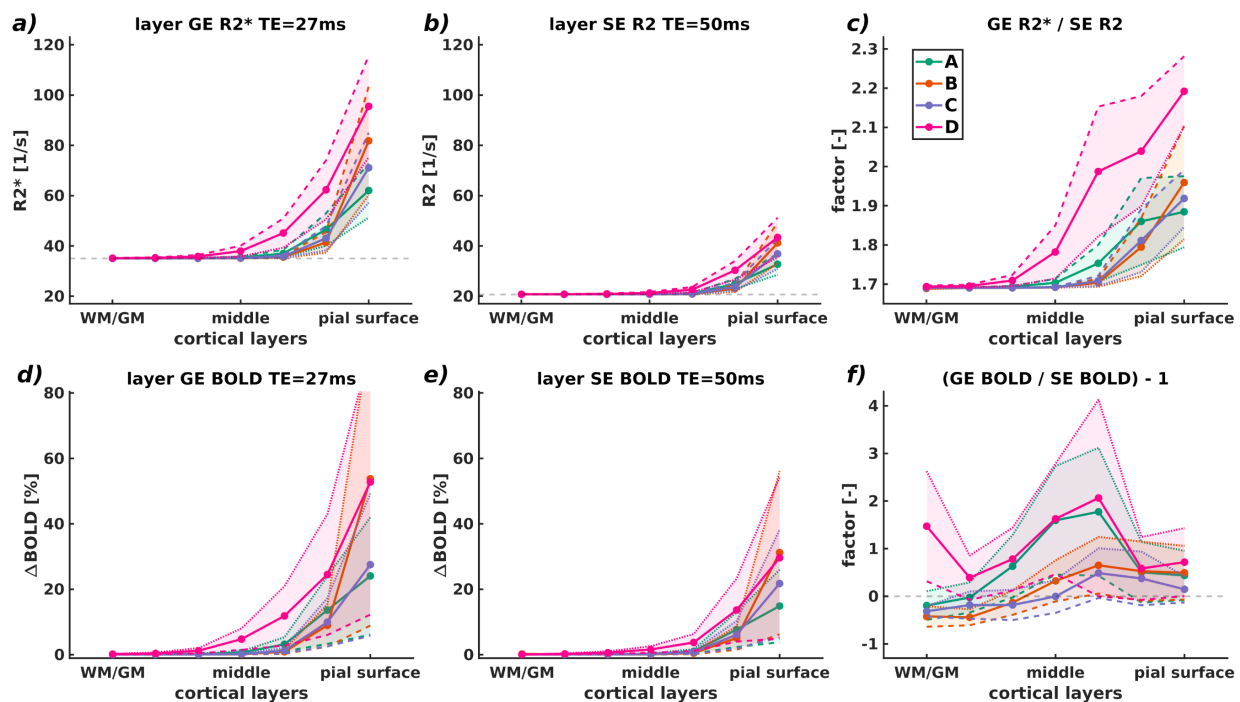


**Figure 4.** The relationship between  $R2^*$  and  $R2$  decay rates (panels **a** – **c**) and BOLD signal changes (panels **d**-**f**) for both GE (TE = 27 ms) and SE (TE = 50 ms) across cortical depth (seven equidistant layers) is depicted for all vascular models. Panels **c**) and **f**) show the resulting GE  $R2^*$ /SE  $R2$  ratio and the ((GE BOLD/SE BOLD) – 1) ratio, respectively. The solid lines represent mean values across all oxygen saturation levels, with shaded areas indicating 95% confidence intervals computed by Monte Carlo simulations. The dashed line indicates the boundary corresponding to the lowest oxygen saturation value, while the dotted line represents the boundary corresponding to the highest oxygen saturation value. The horizontal dashed line in panels **a**) and **b**) corresponds to the intrinsic  $R2_0(^*)$  of tissue. The bottom row panels show solid lines indicating mean BOLD signal change across all oxygen saturation levels, using 59% oxygen saturation state as reference condition ( $SO_{2vein} = 59\%$ ). Shaded areas represent 95% confidence intervals. GE  $R2^*$  values were larger near cortical pial surface, decreasing toward deeper layers. SE  $R2$  exhibited similar trend to GE

439 *R2\* but was reduced/damped by refocusing pulse. Notably, the refocusing pulse did not entirely eliminate*  
 440 *the contribution of large vessels at cortical pial surface.*

441

442 In **Figure 5**, the dependence of  $R2^{(*)}$  decay rates across different echo times for the seven equidistant  
 443 cortical layers is shown for all vascular models. Each solid line in the results represents the mean value,  
 444 while the shaded area indicates the 95% confidence interval averaged across all the oxygen saturation  
 445 levels. The  $R2^{(*)}$  decay rates of the cortical pial surface exhibit the most significant impact on the laminar  
 446 MR signal compared to deeper cortical layers, for both GE and SE sequences. It is notable that SE  $R2$   
 447 reaches a steady-state for all cortical layers at longer echo times, with its value dependent on cortical depth.  
 448 Closer proximity to the pial surface corresponds to higher  $R2^{(*)}$  values. In contrast, GE  $R2^*$  of the pial surface  
 449 layer exhibits lower values for longer echo times, underscoring its dependence on the sequence parameters.  
 450 Additionally, the confidence intervals for both GE  $R2^*$  and SE  $R2$  are wider for superficial layers than deeper  
 451 layers. For layers deeper than the middle layer, neither GE  $R2^*$  nor SE  $R2$  demonstrate considerable  
 452 changes relative to the intrinsic  $R2_0^{(*)}$  of the tissue, respectively.

453

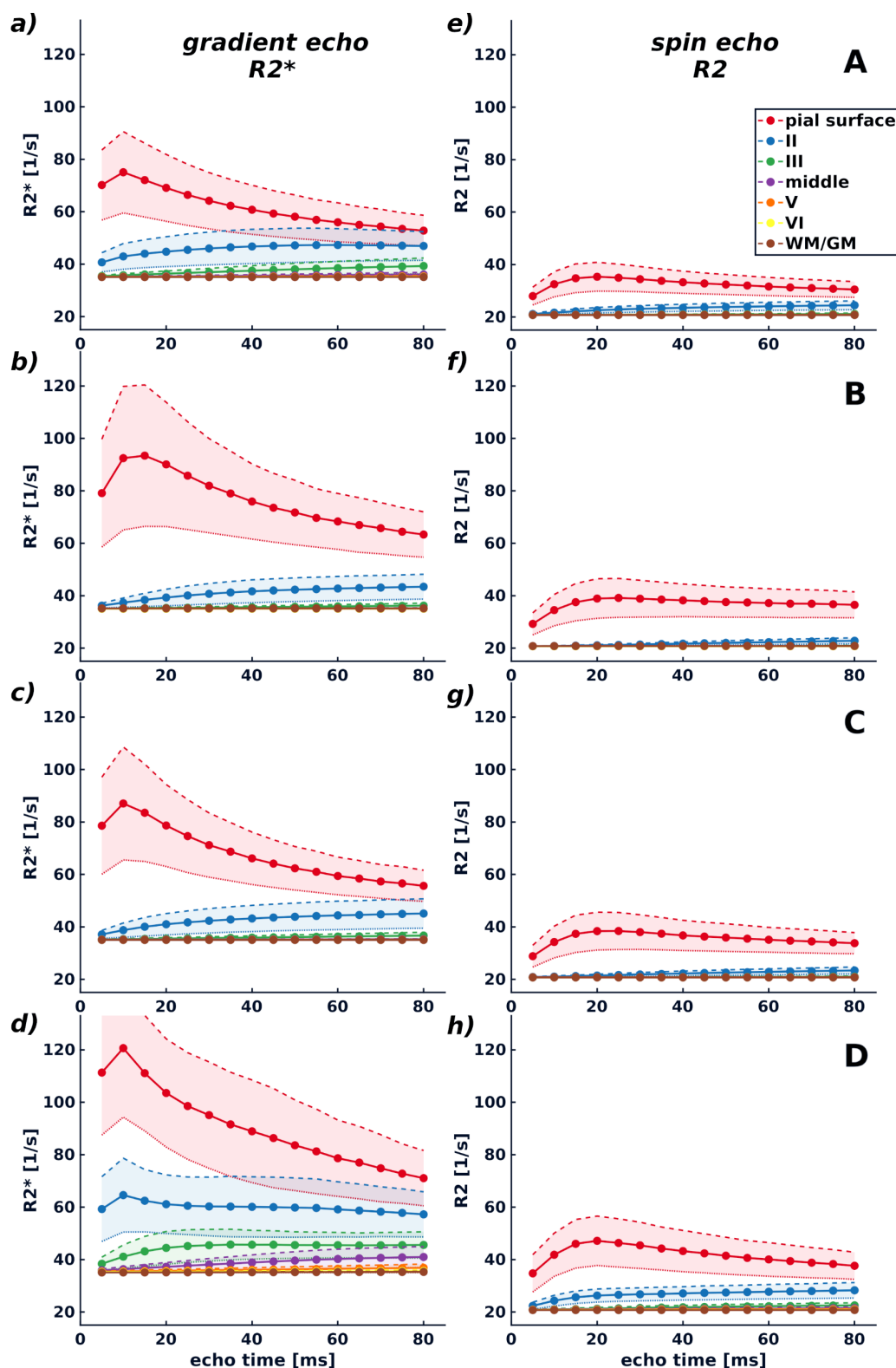


**Figure 5.** Layer GE  $R2^*$  and SE  $R2$  and its dependence on echo time. The correlation between  $R2^{(*)}$  decay rates at different echo times across seven equidistant cortical layers for all vascular models is shown. Each

*solid line in the graphs represents the mean value, while the shaded area indicates the 95% confidence interval using all oxygen saturation states. The decay rates of  $R2^{(*)}$  at the cortical pial surface have the most pronounced impact on the MR signal contribution compared to deeper cortical layers, evident in both GE and SE sequences. Consistent with previous observations, GE  $R2^*$  shows larger values than SE  $R2$ . Notably, SE  $R2$  stabilizes across all cortical layers with longer echo times, its value varying with cortical depth. Proximity to the pial surface correlates with higher GE  $R2^*$  values. Conversely, GE  $R2^*$  displays a slight decrease across echo times at the pial surface layer, emphasizing its reliance on the choice of echo time in sequence parameter selection. Moreover, the confidence interval for both GE  $R2^*$  and SE  $R2$  is broader for superficial layers compared to deeper layers. From the middle to deeper layers, neither GE  $R2^*$  nor SE  $R2$  exhibits substantial changes relative to the tissue's intrinsic  $R2_0^{(*)}$ .*

In **Figure 6**, we show the BOLD signal changes for different echo times across cortical depth for all vascular models. Each solid line in the results represents the mean value, while the shaded area indicates the 95% confidence interval averaged across all the oxygen saturation levels. Notably, the cortical pial surface layer shows the most prominent BOLD signal change for both GE and SE, followed by the layer labeled with the number II and III. The rest of the deeper cortical layers (IV to WM/GM) present similar behaviors across models, except for the D model, which displays a relatively larger contribution from deeper layers. SE BOLD signal changes display comparable, to certain degree, behavior for all vascular models.

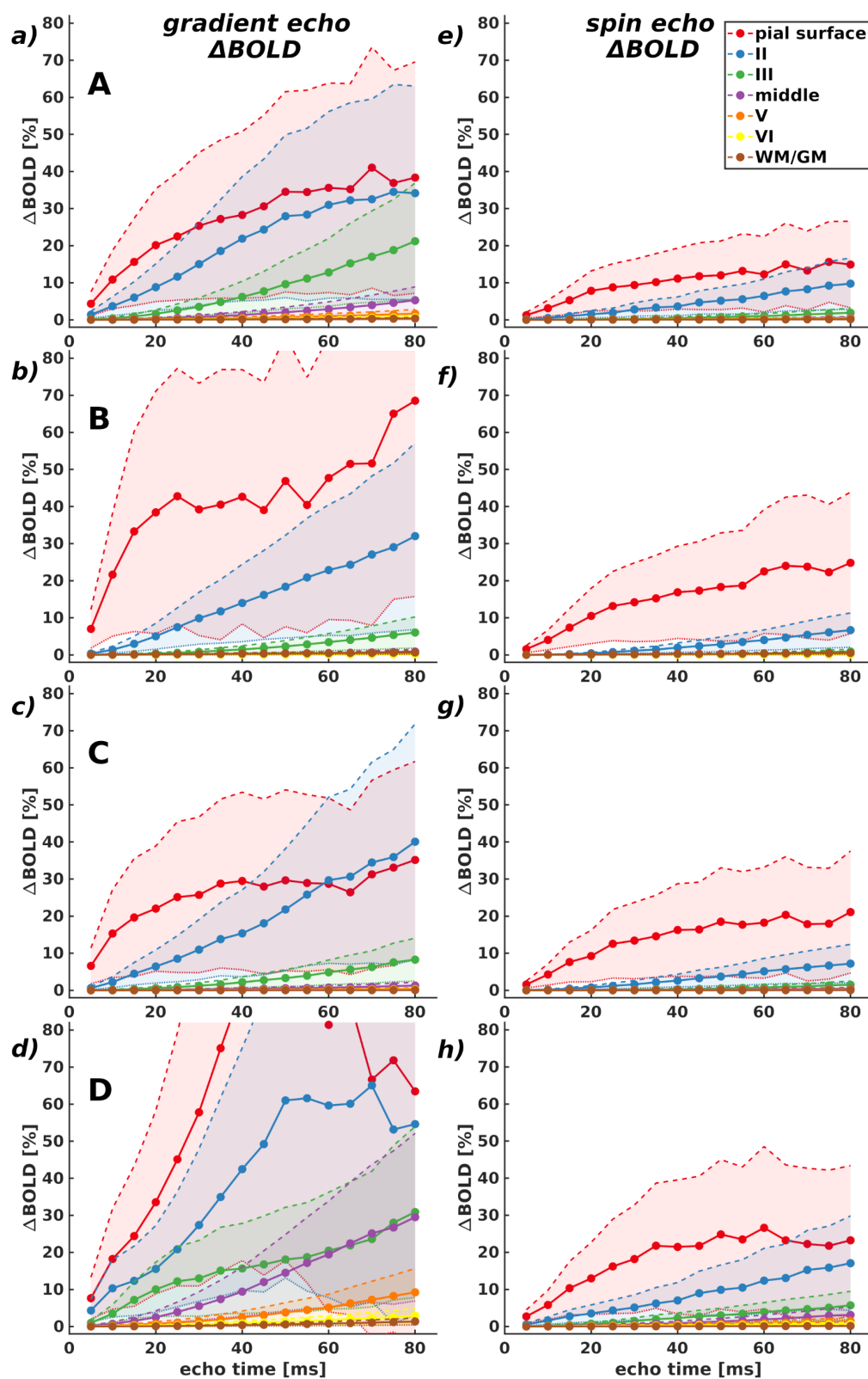


**Figure 6.** GE BOLD and SE BOLD signal changes across different echo times. The variations in BOLD signal across cortical depth and different echo times are examined for all (A - D) vascular models. Each



*solid line in the graphs represents the mean value, while the shaded area indicates the 95% confidence interval averaged across all the oxygen saturation levels. The cortical pial surface exhibits the most substantial BOLD signal change for both GE and SE, followed by the layer labeled with the number II and III. The remaining deeper cortical laminae (IV to WM/GM) exhibit similar behaviors across models, with the exception of the D model, which demonstrates a comparatively larger contribution from deeper layers.*

## **4. DISCUSSION**

### **4.1 General discussion**

In this study, our aim was to characterize the contribution of diverse vascular architectures to  $R2^{(*)}$  and BOLD signal changes using gradient echo and spin echo readouts across cortical depths at 7T. We utilize four realistic 3D vascular models derived from two-photon imaging data and by adjusting the artery-vein ratio, we replicate the human cortical vasculature. We simulated specific oxygen saturation states and biophysical interactions and show that the specificity and signal amplitude of BOLD signals at 7T are determined by the spatial distribution of large vessels across cortical depth and on the pial surface. Our simulations indicate that spin echo BOLD imaging cannot fully mitigate the macrovascular contribution near the cortical pial surface. Additionally, we find that the intravascular contribution, stemming from both arteries and veins, is not negligible in spin echo acquisitions, particularly at high oxygen saturation levels.

Simulations using these realistic 3D vascular models reveal that  $R2^{(*)}$  values and BOLD signal changes are influenced by extravascular and intravascular contributions across cortical depth for both GE and SE sequences. GE  $R2^{(*)}$  values and BOLD signal changes exhibit an increase near the pial surface, mirrored by SE  $R2$  decay rates and BOLD signal changes, although to a lesser extent due to the refocusing 180-degree pulse. Interestingly, the refocusing pulse did not entirely eliminate the contribution of large vessels at the pial surface, indicating that SE BOLD may not fully mitigate macrovascular effects near this cortical layer. Furthermore, our results suggest that the vascular architecture deeper in gray matter, predominantly comprising microvessels, has a relatively minor impact on the laminar signatures of both BOLD signal changes and  $R2^{(*)}$ , resulting in comparable outcomes across the four vascular models. Additionally, specific CBV values for micro- and macrovasculature vary with voxel size and position within the voxel. Hence, based on our simulation results, we conclude that the specificity and signal amplitude of BOLD fMRI signals, whether obtained using spin or gradient echo sequences, are primarily determined by the spatial distribution of large vessels across cortical depth and on the cortical pial surface

### **4.2 Diverse vascular architecture affects the BOLD fMRI signal formation**

The vascular architectures used are composed of arteries, microvessels (capillaries, small arterioles/venules), and veins. The capillary bed within the four models exhibits similar vascular properties,

e.g., vessel radius, relatively similar baseline CBV and vessel density across cortical depth (see **Figure 1**), and to a certain degree, comparable topologies. It is important to note that the vascular architectures were obtained from the same cortical region (parietal), but different mice. The microvascular similarities suggest that, despite the limited number of vascular models, the MR signal contribution from this compartment is comparable across simulations as demonstrated by the relative similar patterns in frequency shifts at the middle plane (see **Figure 2**). The macrovascular architecture is different in all models. This make evident that the diverse topology of the large vessels has a high impact on the MRI signal formation in a voxel, as demonstrated in the inhomogeneous frequency shifts at the top plane (see **Figure 2**), and thus, the contribution from large vessels might not be generalizable, particularly at high spatial resolutions.

It has been previously recognized that the initial phase of the MR signal decay diverges from a mono-exponential curve, as noted in studies such as those by Yablonskiy et al., [2010]<sup>38</sup>, Kiselev et al., [1999]<sup>30</sup>. Our simulations have validated this observation. The global  $R2^{(*)}$  decay values at the voxel level across the four vascular models consistently demonstrated a nonlinear response to changes in oxygen saturation for both gradient echo and spin echo readout techniques at 7T (**Figure 3**). However, SE R2 presents a smaller dephasing effect compared to GE R2\* due to the effect of the 180-degree radiofrequency refocusing pulse. The variations in the computed  $R2^{(*)}$  behavior concerning oxygen saturation among the models can be attributed to differences in their vascular structure. As mentioned earlier, significant differences in the topology of the macrovasculature are observed, while the microvasculature shows almost comparable features across all vascular models which results in similar local inhomogeneous magnetic fields. Simulations using the mono-sized randomly placed and oriented cylinder models<sup>24</sup> show that large vessel contribution is still present in the SE BOLD signal change but reduced as compared with the GE BOLD signal change within the plausible physiological oxygen saturation range as shown in the **Supplementary Figure 2**.

### **4.3 The laminar BOLD fMRI signal is dependent on pulse sequence selection and its imaging parameters**

GE R2\* decay rates show an increase towards the cortical pial surface. SE R2 decay rates follow a similar pattern to GE R2\*, increasing towards the cortical pial surface, albeit to a lesser extent due to the refocusing 180-degree pulse. However, even with the refocusing pulse, the influence of large vessels at the cortical pial surface remains significant. In the deeper layers, most of the contributions to GE R2\* and SE R2 originate from the tissue's  $R2_0^{(*)}$ , accounting a small weighted contribution from extravascular and intravascular CBV and small contributions from R2'. Our findings suggest that the diverse vascular architecture in deeper gray matter has a diminished effect on the laminar signatures of both BOLD signal changes and  $R2^{(*)}$  decay rates. Specifically, the variability in the amplitude of BOLD signal changes and  $R2^{(*)}$  decay rates is reduced in deeper layers, enabling more reliable comparisons of laminar data across individuals or conditions. Nonetheless, minor differences persist even in deeper layers. On the other hand,

superficial layers (pial surface) exhibit significant differences in the topology of the large vessels, leading to a less uniform fingerprint BOLD signal change in these layers. However, these simulation results support the necessity of addressing the bias of large vessels toward the pial surface in laminar fMRI data, for example, through filtering and/or normalization techniques<sup>51,56</sup>.

The choice of echo time in both pulse sequences impacts the contribution of BOLD signals across cortical depth. Overall, our results suggest that the largest BOLD signal contribution at different echo times is observed in the cortical layers near the superficial layer, i.e the pial surface. However, this contribution depends on the topology of the vascular architecture, as middle layers can also play a significant role in generating the BOLD contrast at particular echo times.

#### **4.4 Methodological considerations**

The BOLD signal is affected by alterations in local CBF, CBV, and CMRO<sub>2</sub>. In this study, we have focused solely on simulating the effects of various oxygen saturation states. However, it is important to incorporate changes in cerebral blood volume in future investigations, as variations in CBV significantly influence R2(\*) decay values and, consequently, the BOLD signal change<sup>13,38,46,47</sup>.

Furthermore, this encourages deeper exploration of the complex relationship between neural activity, hemodynamic response, and the unique characteristics of cortical layers. While our study introduced a more realistic vascular architectural model to assess its impact on the BOLD signal across cortical depth, we noted the relative simplicity of our hemodynamic model. Acknowledging this limitation, we recognize the necessity of adopting a more sophisticated hemodynamic model for future advancements. Advancing our understanding of hemodynamic processes will refine simulations by incorporating factors like blood flow dynamics, oxygen transport, and metabolic regulation, leading to a more comprehensive representation of vascular function and its influence on imaging signals<sup>45,55</sup>.

The calculation of the BOLD signal change in this study focuses on the extravascular and intravascular signal contribution. The extravascular component arises from the interaction between diffusing spins and magnetic field changes due to susceptibility differences in the vascular compartments and due to differential oxygen saturation levels. The intravenous contribution to the BOLD signal might be disregarded for GE readouts due to the relatively short T2\*<sub>0</sub> relaxation time constant of oxygenated blood at ultra-high magnetic fields, as indicated by Uludağ et. al. [2009]<sup>29</sup>. While the intravascular contribution of both arterial and venous components may be negligible for GE sequences, the intravascular component of the arterial compartment is demonstrated to play an important role in SE sequences at 7T.

It has been demonstrated that the specificity of the SE acquisition scheme has a clear dependence on the echo train length used to encode the signal using EPI readouts<sup>31,32</sup>. In this work we presumed signal acquisition without any influence of the imaging gradients—duration of spatial position encoding is neglected.

Thus, different parameter selection in the EPI readouts may influence the behavior of the  $R2^{(*)}$  and the corresponding BOLD signal changes<sup>32</sup>.

The vascular specificity of SE  $R2$  also depends on the assumed diffusion coefficient. The diffusion coefficient at the GM/CSF boundary (superficial pial layer) might influence the computed BOLD signal changes due to the faster diffusional motion of water molecules in the CSF compartment. Future simulations should take into account these two diffusion motion regimes<sup>38,48</sup>.

The fluctuation in the amplitude of the BOLD signal concerning the angular orientation of the main magnetic field is significantly influenced by the orientation of the vasculature, as supported by previous studies in human subjects<sup>12,54</sup> and simulations<sup>45,58</sup>. This angular dependency is directly attributed to both pial vessels and penetrating/ascending vessels. Therefore, we envision future studies to demonstrate the laminar variability in the amplitude of the BOLD signal depending on various oxygen saturation levels.

A limitation of the current study is the arbitrary labeling of the large vessels. Here, we enforced an assumed human artery/vein ratio for labeling the macrovessels. While this ratio was consistent across all models, the specific selection of certain vessels might influence the behavior of the laminar profile across cortical depth.

Likewise, it's crucial to consider the disparity in cortical thickness between mice and humans<sup>39,45,53</sup>, though this does not influence the simulation conclusions reported here. Nevertheless, we anticipate improving our computational model to account for this disparity. One prospective method could entail virtually generating synthetic 3D vascular networks<sup>45</sup>, incorporating statistical characteristics of both macrovessels and microvessels, which span approximately ~2-3 mm in cortical depth and maintain an artery-venous ratio consistent with the cortical properties of a specific brain region<sup>53</sup>.

## 4.5 Conclusion

We observe that GE  $R2^{*}$  decay rates follow an increasing trend towards the cortical pial surface, peaking near this layer, and demonstrate a decreasing trend towards the deeper layers. In the deeper layers, the majority of the  $R2^{(*)}$  contribution originates from the tissue's intrinsic  $R2^{(*)}0$ . SE  $R2$  decay rates exhibit a similar pattern to GE  $R2^{*}$  with increasing values towards the cortical pial surface; however, they are smaller due to the presence of the refocusing 180-degree pulse. Despite the inclusion of the refocusing pulse, the contribution of large vessels at the cortical pial surface remains significant. This pattern is similar for the BOLD signal changes. Therefore, the diverse topology of large vessels influences the relative sensitivity of the MRI signal to different layers, and the reliance on specific models suggests that contributions from large vessels may not be generalizable. Furthermore, while the vascular compartments remain consistent across the four vascular models, variations in vascular topology, particularly in the macrovasculature, result in differences in computed  $R2^{(*)}$  effects and BOLD signal changes. Thus, the use of multiple realistic 3D vascular models is necessary in studies exploring the relationship between angioarchitecture and the biophysical effects on the human fingerprint BOLD fMRI signal formation. This computational approach

helps in understanding the influence of the vascular architecture on GE BOLD and SE BOLD signal formation across cortical depth, as well as the impact of pulse sequence parameter selection on BOLD signal changes at submillimeter acquisitions.

## ACKNOWLEDGEMENTS

This work was supported by the National Institute of Mental Health of the National Institutes of Health under the Award Number R01MH111417 and the Dutch Research Council under award number 18969. The content is solely the responsibility of the authors and does not necessarily represent the official views of the National Institutes of Health.

## AUTHOR CONTRIBUTION STATEMENT

MGBY, JS and NP: conceived and designed the project. NP and MvO: obtained funding to support the project. MGBY: developed the computational pipeline, run the simulations, designed the figures and wrote the original draft of the manuscript. VC: performed the labelling of the vessels and analyzed the vascular data. All authors discussed the results and reviewed and edited the manuscript.

## DISCLOSURE/CONFLICT OF INTEREST

The authors declare that they have no known competing financial interests, conflict of interest or personal relationships that could have appeared to influence the work reported in this paper.

## CODE/DATA AVAILABILITY STATEMENT

The code and data underlying the findings of this study are available from the corresponding author upon request. Access is subject to a nonexclusive, revocable, non-transferable, and limited right to use solely for research and evaluation purposes, excluding any commercial use.

## REFERENCES

1. Ogawa S, Menon RS, Tank DW, Kim SG, Merkle H, Ellermann JM, Ugurbil K. Functional brain mapping by blood oxygenation level-dependent contrast magnetic resonance imaging. A comparison of signal characteristics with a biophysical model. *Biophys J.* 1993 Mar;64(3):803-12. doi: 10.1016/S0006-3495(93)81441-3. PMID: 8386018; PMCID: PMC1262394.

2. Bandettini PA, Wong EC, Jesmanowicz A, Hinks RS, Hyde JS. Spin-echo and gradient-echo EPI of human brain activation using BOLD contrast: a comparative study at 1.5 T. *NMR Biomed.* 1994 Mar;7(1-2):12-20. doi: 10.1002/nbm.1940070104. PMID: 8068520.
3. Bandettini PA, Kwong KK, Davis TL, Tootell RB, Wong EC, Fox PT, Belliveau JW, Weisskoff RM, Rosen BR. Characterization of cerebral blood oxygenation and flow changes during prolonged brain activation. *Hum Brain Mapp.* 1997;5(2):93-109. PMID: 10096414.
4. Huber L, Handwerker DA, Jangraw DC, Chen G, Hall A, Stüber C, Gonzalez-Castillo J, Ivanov D, Marrett S, Guidi M, Goense J, Poser BA, Bandettini PA. High-Resolution CBV-fMRI Allows Mapping of Laminar Activity and Connectivity of Cortical Input and Output in Human M1. *Neuron.* 2017 Dec 20;96(6):1253-1263.e7. doi: 10.1016/j.neuron.2017.11.005. Epub 2017 Dec 7. PMID: 29224727; PMCID: PMC5739950.
5. Kashyap S, Ivanov D, Havlicek M, Poser BA, Uludağ K. Impact of acquisition and analysis strategies on cortical depth-dependent fMRI. *Neuroimage.* 2018 Mar; 168:332-344. doi: 10.1016/j.neuroimage.2017.05.022. Epub 2017 May 12. PMID: 28506874.
6. Nasr S, Polimeni JR, Tootell RB. Interdigitated Color- and Disparity-Selective Columns within Human Visual Cortical Areas V2 and V3. *J Neurosci.* 2016 Feb 10;36(6):1841-57. doi: 10.1523/JNEUROSCI.3518-15.2016. PMID: 26865609; PMCID: PMC4748071.
7. Norris DG, Polimeni JR. Laminar (f)MRI: A short history and future prospects. *Neuroimage.* 2019 Aug 15; 197:643-649. doi: 10.1016/j.neuroimage.2019.04.082. Epub 2019 May 3. PMID: 31059800.
8. Olman CA, Harel N, Feinberg DA, He S, Zhang P, Ugurbil K, Yacoub E. Layer-specific fMRI reflects different neuronal computations at different depths in human V1. *PLoS One.* 2012;7(3):e32536. doi: 10.1371/journal.pone.0032536. Epub 2012 Mar 20. PMID: 22448223; PMCID: PMC3308958.
9. Polimeni JR, Uludağ K. Neuroimaging with ultra-high field MRI: Present and future. *Neuroimage.* 2018 Mar; 168:1-6. doi: 10.1016/j.neuroimage.2018.01.072. Epub 2018 Feb 1. PMID: 29410013.
10. Puckett AM, Aquino KM, Robinson PA, Breakspear M, Schira MM. The spatiotemporal hemodynamic response function for depth-dependent functional imaging of human cortex. *Neuroimage.* 2016 Oct 1; 139:240-248. doi: 10.1016/j.neuroimage.2016.06.019. Epub 2016 Jun 15. PMID: 27321045.
11. Siero JC, Petridou N, Hoogduin H, Luijten PR, Ramsey NF. Cortical depth-dependent temporal dynamics of the BOLD response in the human brain. *J Cereb Blood Flow Metab.* 2011 Oct;31(10):1999-2008. doi: 10.1038/jcbfm.2011.57. Epub 2011 Apr 20. PMID: 21505479; PMCID: PMC3208150.
12. Fracasso A, Luijten PR, Dumoulin SO, Petridou N. Laminar imaging of positive and negative BOLD in human visual cortex at 7T. *Neuroimage.* 2018 Jan 1; 164:100-111. doi: 10.1016/j.neuroimage.2017.02.038. Epub 2017 Feb 14. PMID: 28213112.
13. Dumoulin SO, Fracasso A, van der Zwaag W, Siero JCW, Petridou N. Ultra-high field MRI: Advancing systems neuroscience towards mesoscopic human brain function. *Neuroimage.* 2018 Mar; 168:345-357. doi: 10.1016/j.neuroimage.2017.01.028. Epub 2017 Jan 16. PMID: 28093360.



14. Markuerkiaga I, Marques JP, Bains LJ, Norris DG. An in-vivo study of BOLD laminar responses as a function of echo time and static magnetic field strength. *Sci Rep.* 2021 Jan 21;11(1):1862. doi: 10.1038/s41598-021-81249-w. PMID: 33479362; PMCID: PMC7820587.
15. De Martino F, Zimmermann J, Muckli L, Ugurbil K, Yacoub E, Goebel R. Cortical depth dependent functional responses in humans at 7T: improved specificity with 3D GRASE. *PLoS One.* 2013;8(3):e60514. doi: 10.1371/journal.pone.0060514. Epub 2013 Mar 22. PMID: 23533682; PMCID: PMC3606277.
16. Gau R, Bazin PL, Trampel R, Turner R, Noppeney U. Resolving multisensory and attentional influences across cortical depth in sensory cortices. *Elife.* 2020 Jan 8;9:e46856. doi: 10.7554/eLife.46856. PMID: 31913119; PMCID: PMC6984812.
17. Kok P, Bains LJ, van Mourik T, Norris DG, de Lange FP. Selective Activation of the Deep Layers of the Human Primary Visual Cortex by Top-Down Feedback. *Curr Biol.* 2016 Feb 8;26(3):371-6. doi: 10.1016/j.cub.2015.12.038. Epub 2016 Jan 28. PMID: 26832438.
18. Zaldivar D, Rauch A, Logothetis NK, Goense J. Two distinct profiles of fMRI and neurophysiological activity elicited by acetylcholine in visual cortex. *Proc Natl Acad Sci U S A.* 2018 Dec 18;115(51):E12073-E12082. doi: 10.1073/pnas.1808507115. Epub 2018 Dec 3. PMID: 30510000; PMCID: PMC6304994.
19. Siero JC, Ramsey NF, Hoogduin H, Klomp DW, Luijten PR, Petridou N. BOLD specificity and dynamics evaluated in humans at 7 T: comparing gradient-echo and spin-echo hemodynamic responses. *PLoS One.* 2013;8(1):e54560. doi: 10.1371/journal.pone.0054560. Epub 2013 Jan 15. PMID: 23336008; PMCID: PMC3546000.
20. Petridou N, Siero JCW. Laminar fMRI: What can the time domain tell us? *Neuroimage.* 2019 Aug 15; 197:761-771. doi: 10.1016/j.neuroimage.2017.07.040. Epub 2017 Jul 20. PMID: 28736308; PMCID: PMC5775945.
21. Kotlarz P, Lankinen K, Hakonen M, Turpin T, Polimeni JR, Ahveninen J. Multilayer Network Analysis across Cortical Depths in Resting-State 7T fMRI. *bioRxiv [Preprint].* 2023 Dec 23:2023.12.23.573208. doi: 10.1101/2023.12.23.573208. PMID: 38187540; PMCID: PMC10769454
22. Bause J, Polimeni JR, Stelzer J, In MH, Ehses P, Kraemer-Fernandez P, Aghaeifar A, Lacosse E, Pohmann R, Scheffler K. Impact of prospective motion correction, distortion correction methods and large vein bias on the spatial accuracy of cortical laminar fMRI at 9.4 Tesla. *Neuroimage.* 2020 Mar; 208:116434. doi: 10.1016/j.neuroimage.2019.116434. Epub 2019 Dec 6. PMID: 31812715.
23. Han S, Eun S, Cho H, Uludağ K, Kim SG. Improved laminar specificity and sensitivity by combining SE and GE BOLD signals. *Neuroimage.* 2022 Dec 1; 264:119675. doi: 10.1016/j.neuroimage.2022.119675. Epub 2022 Oct 13. PMID: 36243267.
24. Polimeni JR, Fischl B, Greve DN, Wald LL. Laminar analysis of 7T BOLD using an imposed spatial activation pattern in human V1. *Neuroimage.* 2010 Oct 1;52(4):1334-46. doi: 10.1016/j.neuroimage.2010.05.005. Epub 2010 May 9. PMID: 20460157; PMCID: PMC3130346.



25. Stephan KE, Petzschner FH, Kasper L, Bayer J, Wellstein KV, Stefanics G, Pruessmann KP, Heinze J. Laminar fMRI and computational theories of brain function. *Neuroimage*. 2019 Aug 15; 197:699-706. doi: 10.1016/j.neuroimage.2017.11.001. Epub 2017 Nov 2. PMID: 29104148
26. Dumoulin SO. Layers of Neuroscience. *Neuron*. 2017 Dec 20;96(6):1205-1206. doi: 10.1016/j.neuron.2017.12.004. PMID: 29268088.
27. Choi S, Zeng H, Chen Y, Sobczak F, Qian C, Yu X. Laminar-specific functional connectivity mapping with multi-slice line-scanning fMRI. *Cereb Cortex*. 2022 Oct 8;32(20):4492-4501. doi: 10.1093/cercor/bhab497. Erratum in: *Cereb Cortex*. 2023 Mar 21;33(7):4188. PMID: 35107125; PMCID: PMC9574235.
28. Weisskoff RM, Zuo CS, Boxerman JL, Rosen BR. Microscopic susceptibility variation and transverse relaxation: theory and experiment. *Magn Reson Med*. 1994 Jun;31(6):601-10. doi: 10.1002/mrm.1910310605. PMID: 8057812.
29. Boxerman JL, Hamberg LM, Rosen BR, Weisskoff RM. MR contrast due to intravascular magnetic susceptibility perturbations. *Magn Reson Med*. 1995 Oct;34(4):555-66. doi: 10.1002/mrm.1910340412. PMID: 8524024.
30. Kiselev VG, Posse S. Analytical model of susceptibility-induced MR signal dephasing: effect of diffusion in a microvascular network. *Magn Reson Med*. 1999 Mar;41(3):499-509. doi: 10.1002/(sici)1522-2594(199903)41:3<499:aid-mrm12>3.0.co;2-o. PMID: 10204873.
31. Kiselev VG. On the theoretical basis of perfusion measurements by dynamic susceptibility contrast MRI. *Magn Reson Med*. 2001 Dec;46(6):1113-22. doi: 10.1002/mrm.1307. PMID: 11746577.
32. Norris DG. Spin-echo fMRI: The poor relation? *Neuroimage*. 2012 Aug 15;62(2):1109-15. doi: 10.1016/j.neuroimage.2012.01.003. Epub 2012 Jan 8. PMID: 22245351.
33. Uludağ K, Müller-Bierl B, Uğurbil K. An integrative model for neuronal activity-induced signal changes for gradient and spin echo functional imaging. *Neuroimage*. 2009 Oct 15;48(1):150-65. doi: 10.1016/j.neuroimage.2009.05.051. Epub 2009 May 27. PMID: 19481163.
34. Pfaffenrot V, Voelker MN, Kashyap S, Koopmans PJ. Laminar fMRI using T2-prepared multi-echo FLASH. *Neuroimage*. 2021 Aug 1; 236:118163. doi: 10.1016/j.neuroimage.2021.118163. Epub 2021 May 21. PMID: 34023449.
35. Goense JB, Logothetis NK. Laminar specificity in monkey V1 using high-resolution SE-fMRI. *Magn Reson Imaging*. 2006 May;24(4):381-92. doi: 10.1016/j.mri.2005.12.032. Epub 2006 Mar 13. PMID: 16677944.
36. Van Horen TWP, Siero JCW, Bhogal AA, Petridou N, Báez-Yáñez MG. Microvascular Specificity of Spin Echo BOLD fMRI: Impact of EPI Echo Train Length. *bioRxiv* [Preprint]. 2023 Sep 15:2023.09.15.557938. doi: 10.1101/2023.09.15.557938. PMID: 37745507; PMCID: PMC10516014.
37. Havlicek M, Ivanov D, Poser BA, Uludag K. Echo-time dependence of the BOLD response transients - A window into brain functional physiology. *Neuroimage*. 2017 Oct 1; 159:355-370. doi: 10.1016/j.neuroimage.2017.07.034. Epub 2017 Jul 18. PMID: 28729160.

38. Yablonskiy DA, Sukstanskii AL. Theoretical models of the diffusion weighted MR signal. *NMR Biomed.* 2010 Aug;23(7):661-81. doi: 10.1002/nbm.1520. PMID: 20886562; PMCID: PMC6429954.
39. Blinder P, Tsai PS, Kaufhold JP, Knutsen PM, Suhl H, Kleinfeld D. The cortical angiome: an interconnected vascular network with noncolumnar patterns of blood flow. *Nat Neurosci.* 2013 Jul;16(7):889-97. doi: 10.1038/nn.3426. Epub 2013 Jun 9. PMID: 23749145; PMCID: PMC4141079.
40. Schmid F, Barrett MJP, Jenny P, Weber B. Vascular density and distribution in neocortex. *Neuroimage.* 2019 Aug 15; 197:792-805. doi: 10.1016/j.neuroimage.2017.06.046. Epub 2017 Jun 29. PMID: 28669910.
41. Duvernoy HM, Delon S, Vannson JL. Cortical blood vessels of the human brain. *Brain Res Bull.* 1981 Nov ;7(5):519-79. doi: 10.1016/0361-9230(81)90007-1. PMID : 7317796.
42. Uludağ K, Blinder P. Linking brain vascular physiology to hemodynamic response in ultra-high field MRI. *Neuroimage.* 2018 Mar; 168:279-295. doi: 10.1016/j.neuroimage.2017.02.063. Epub 2017 Feb 22. PMID: 28254456.
43. Stamenkovic S, Schmid F, Weitermann N, Takasaki K, Bonney SK, Sosa MJ, Li Y, Bennett HC, Kim Y, Waters J, Shih AY. Impaired drainage through capillary-venous networks contributes to age-related white matter loss. *bioRxiv [Preprint].* 2024 Feb 12:2024.02.11.579849. doi: 10.1101/2024.02.11.579849. PMID: 38405879; PMCID: PMC10888936.
44. Báez-Yáñez MG, Ehses P, Mirkes C, Tsai PS, Kleinfeld D, Scheffler K. The impact of vessel size, orientation and intravascular contribution on the neurovascular fingerprint of BOLD bSSFP fMRI. *Neuroimage.* 2017 Dec; 163:13-23. doi: 10.1016/j.neuroimage.2017.09.015. Epub 2017 Sep 8. PMID: 28890417; PMCID: PMC5857886.
45. Báez-Yáñez M.G., Siero JCW, Petridou N. A mechanistic computational framework to investigate the hemodynamic fingerprint of the blood oxygenation level-dependent signal. *NMR Biomed.* 2023 Aug 29: e5026
46. Kiselev VG, Novikov DS. Transverse NMR relaxation in biological tissues. *Neuroimage.* 2018 Nov 15; 182:149-168. doi: 10.1016/j.neuroimage.2018.06.002. Epub 2018 Jun 7. PMID: 29885485; PMCID: PMC6175675.
47. Khajehim M, Nasiraei Moghaddam A. Investigating the spatial specificity of S2-SSFP fMRI: A Monte Carlo simulation approach. *Magn Reson Imaging.* 2017 Apr; 37:282-289. doi: 10.1016/j.mri.2016.11.016. Epub 2016 Nov 24. PMID: 27890778.
48. Sanchez Panchuelo RM, Schluppeck D, Harmer J, Bowtell R, Francis S. Assessing the spatial precision of SE and GE-BOLD contrast at 7 Tesla. *Brain Topogr.* 2015 Jan;28(1):62-5. doi: 10.1007/s10548-014-0420-4. Epub 2014 Dec 10. PMID: 25491676.
49. Pfaffenrot V, Koopmans PJ. Magnetization transfer weighted laminar fMRI with multi-echo FLASH. *Neuroimage.* 2022 Dec 1; 264:119725. doi: 10.1016/j.neuroimage.2022.119725. Epub 2022 Oct 31. PMID: 36328273.

50. Báez-Yáñez M.G., Schellekens W, Bhogal AA, Siero JC, Petridou N. Numerical simulations to investigate the contribution of arteries and veins to the relative BOLD-fMRI signal change by means of SO<sub>2</sub> and CBV changes. Proc ISMRM (2021) abstract: #3399
51. Schellekens W, Bhogal AA, Roefs EC, Báez-Yáñez MG, Siero JC, Petridou N. The many layers of BOLD. The effect of hypercapnic and hyperoxic stimuli on macro- and micro-vascular compartments quantified by CVR, M, and CBV across cortical depth. J Cereb Blood Flow Metab. 2023 Mar;43(3):419-432. doi: 10.1177/0271678X221133972. Epub 2022 Oct 19. PMID: 36262088; PMCID: PMC9941862.
52. Pflugfelder D, Vahedipour K, Uludağ K, Shah NJ, Stöcker T. On the numerically predicted spatial BOLD fMRI specificity for spin echo sequences. Magn Reson Imaging. 2011 Nov;29(9):1195-204. doi: 10.1016/j.mri.2011.07.015. Epub 2011 Sep 13. PMID: 21917392.
53. Vovenko E. Distribution of oxygen tension on the surface of arterioles, capillaries and venules of brain cortex and in tissue in normoxia: an experimental study on rats. Pflugers Arch. 1999 Mar;437(4):617-23. doi: 10.1007/s004240050825. PMID: 10089576.
54. Viessmann O, Scheffler K, Bianciardi M, Wald LL, Polimeni JR. Dependence of resting-state fMRI fluctuation amplitudes on cerebral cortical orientation relative to the direction of B<sub>0</sub> and anatomical axes. Neuroimage. 2019 Aug 1;196:337-350. doi: 10.1016/j.neuroimage.2019.04.036. Epub 2019 Apr 17. PMID: 31002965; PMCID: PMC6559854.
55. Hartung G, Vesel C, Morley R, Alaraj A, Sled J, Kleinfeld D, Linninger A. Simulations of blood as a suspension predicts a depth dependent hematocrit in the circulation throughout the cerebral cortex. PLoS Comput Biol. 2018 Nov 19;14(11):e1006549. doi: 10.1371/journal.pcbi.1006549. PMID: 30452440; PMCID: PMC6277127.
56. Vizioli L, Moeller S, Dowdle L, Akçakaya M, De Martino F, Yacoub E, Uğurbil K. Lowering the thermal noise barrier in functional brain mapping with magnetic resonance imaging. Nat Commun. 2021 Aug 30;12(1):5181. doi: 10.1038/s41467-021-25431-8. PMID: 34462435; PMCID: PMC8405721.
57. Poplawsky AJ, Fukuda M, Kim SG. Foundations of layer-specific fMRI and investigations of neurophysiological activity in the laminarized neocortex and olfactory bulb of animal models. Neuroimage. 2019 Oct 1;199:718-729. doi: 10.1016/j.neuroimage.2017.05.023. Epub 2017 May 12. PMID: 28502845; PMCID: PMC5682230.
58. Gagnon L, Sakadžić S, Lesage F, Musacchia JJ, Lefebvre J, Fang Q, Yücel MA, Evans KC, Mandeville ET, Cohen-Adad J, Polimeni JR, Yaseen MA, Lo EH, Greve DN, Buxton RB, Dale AM, Devor A, Boas DA. Quantifying the microvascular origin of BOLD-fMRI from first principles with two-photon microscopy and an oxygen-sensitive nanoprobe. J Neurosci. 2015 Feb 25;35(8):3663-75. doi: 10.1523/JNEUROSCI.3555-14.2015. PMID: 25716864; PMCID: PMC4339366.
59. Lorthois S, Cassot F, Lauwers F. Simulation study of brain blood flow regulation by intra-cortical arterioles in an anatomically accurate large human vascular network: Part I: methodology and baseline flow. Neuroimage. 2011 Jan 15;54(2):1031-42. doi: 10.1016/j.neuroimage.2010.09.032. Epub 2010 Oct 15. PMID: 20869450.

- 830 60. Weber B, Keller AL, Reichold J, Logothetis NK. The microvascular system of the striate and extrastriate  
831 visual cortex of the macaque. *Cereb Cortex*. 2008 Oct;18(10):2318-30. doi: 10.1093/cercor/bhm259.  
832 Epub 2008 Jan 24. PMID: 18222935.